Long-term simulation of dust distribution with the GOCART model: Correlation with the North Atlantic Oscillation

P. Ginoux [*,1]

GEST, University of Maryland Baltimore County, Maryland, USA

J. Prospero

RSMAS, University of Miami, Florida, USA

O. Torres

JCET, University of Maryland Baltimore County, Maryland, USA

M. Chin

ESA, Georgia Institute of Technology, Georgia, USA

Abstract

Global distribution of aeolian dust is simulated from 1981 to 1996 with the Goddard Ozone Chemistry Aerosol Radiation and Transport (GOCART) model. The results are assessed with in-situ measurements and the Total Ozone Mapping Spectrometer (TOMS) aerosol products. The annual budget over the different continents and oceans are analyzed. It is found that there is a maximum of 25% difference of global anuual emission from the minimum in 1996 to the maximum in 1988. There is a downward trend of dust emission over Africa and East Asia, of 6 and 2 Tg yr-1, respectively. The inter-annual variability of dust distribution is analyzed over the North Atlantic and Africa. It is found that in winter most of the North Atlantic and Africa dust loading is correlated with the North Atlantic Oscillation. The GOCART model indicates that a controlling factor of such correlation can be attributed to dust emission from the Sahel. The Bodele depression is the major dust source in winter and its inter-annual variability is highly correlated with the NAO. However, it is not possible to conclude without further analysis that the North Atlantic Oscillation is forcing the inter-annual variability of dust emission and in-turn dust concentration over the North Atlantic.

Key words: Global modeling, Dust, North Atlantic Oscillation

1 Introduction

Mineral dust has an impact on the different components of the Earth system. Several studies have shown that dust particles, by absorbing and scattering solar radiation, modify the atmospheric radiative budget (e.g. *Tegen et al.* (1996); *Sokolik and Toon* (1996); *Weaver et al.* (2002)). Also, it could play a positive role in reducing global warming by greenhouse gas CO_2. The carbon fixation by phytoplanktons in the oceans acts as a sink for CO_2. Aeolian dust deposition is the primary source of bio-available iron in the iron limited open oceans and effectively control phytoplankton blooming (*Martin and Gordon*, 1988). Another important effect of dust particles is their role in the photochemical production of tropospheric ozone by reducing by as much as 50% the photolysis rates (e.g. *Dickerson et al.* (1997); *Liao et al.* (1999); *Martin et al.* (2002)) and by providing reaction sites for ozone and nitrogen molecules (e.g. *Prospero et al.* (1995); *Dentener et al.* (1996)). Finally, dust particles affect air quality (*Prospero*, 1999) and are potential vectors for long range transport of bacteria (*Griffin et al.*, 2001). It is thus important to better understand the long term variability of dust distributiona and what can be the controling factors of such variability.

In-situ measurements from the 60's have shown strong daily, seasonal and interannual variations of dust concentration over the Atlantic (*Prospero*, 1999). Aerosol satellite data have been helpful to locate the major dust sources (*Herman et al.* (1997); *Prospero et al.* (2002)) and to study the variability of aerosols distribution with data since the 70's (*Herman et al.* (1997); *Torres et al.* (2002)). Also dust sources are located on all continents, North Africa seems to be the most productive with most dust plumes transported to the North Atlantic. In this paper, we will focus on dust emission fron North Africa and dust distribution over the North Atlantic, although they will be compare with emissions from other continents and deposition over other oceans. *Hurrell* (1995) have shown that the circulation and precipitation over Europe and the North Atlantic is modulated by the North Atlantic Oscillation (NAO) with a period of about 8 years. *Moulin et al.* (1997) found a weak correlation between the NAO and the long term variability of in-situ of dust concentration as well as with satellite data. Transport models solve explicitly the emission, transport and removal processes. Therefore, they can provide more detail information on the major processes controlling the spatial and temporal variability of dust distribution. *Ginoux et al.* (2001) have developed a transport model driven by assimilated meteorology which can reproduce successfully dust seasonal variation at the global scale. This paper is focusing on the year-to-year variation of the budget over dif-

ferent continents and oceans, and on its correlation with the NAO. After describing briefly the transport model used to simulate dust distribution, the budget over the continents and oceans will be discussed before comparing the model results with in-situ and remote sensing data. Finally, the effects of the North Atlantic Oscillation on dust emission, concentration and mass column will be analyzed.

2 Model Description

The model uses for this study is the Goddard Ozone Chemistry Aerosol Radiation and Transport (GOCART) model. The GOCART model simulates the distribution of dust, sulfate, carbonaceous (organic and black carbon), and sea-salt aerosols. Each model component has been described in details elsewhere (*Chin et al.* (2000); *Ginoux et al.* (2001); *Chin et al.* (2002)). Here we will briefly describe the dust component of the GOCART model.

Dust size distribution is calculated by solving the continuity equation for a discrete number of size bins. The size distribution of mineral dust extended from 0.1 μm for clay to several hundreds μm for sand. However, the volume (or mass) of particles larger than 10 μm is several orders of magnitude lower than for smaller particles, and the maximum of the volume is around 2 μm radius (*Dubovik et al.,* 2002). The size distribution for particles larger than 1μm is primarly constrained by gravitational settling. In GOCART model, the size distribution is discretized into four size bins: 0.1-1, 1-2, 2-3, 3-6 μm radius. The physical parameters of these 4 bins are given in Table 1. The continuity equation includes macroscopic advection by winds, parameterized eddy diffusion and moist convection. The removal mechanisms include dry deposition at the surface by impaction, wet deposition in and below clouds, and gravitational settling. Dust is uplifted by wind over preferential sources which have been associated with topographic lows. The model has a horizontal resolution of 2° latitude by 2.5° longitude and 20 vertical sigma layers from the surface to 1 mb ($\sim$ 50 km). All processes are driven by assimilated meteorological fields by the Goddard Earth Observing System Data Assimilation System (GEOS DAS) at NASA Goddard (*Schubert et al.,* 1993).

2.1 Dust Sources

The approach used in GOCART to identify the major dust sources is based on the analysis by *Prospero et al.* (2002). Using the Total Ozone Mapping Spectrometer (TOMS) aerosol index (http://toms.gsfc.nasa.gov), they have identified and characterized the geo-morphological nature of the major dust sources. Based on this analysis and the previous work by *Herman et al.* (1997), a global dust-source function has been defined as the probability of sediments accumulated in topographic

3

depressions with bare surface (*Ginoux et al.*, 2001). Figure 1 shows the global distribution of the source function on one dgree grid, and the climatological TOMS absorbing aerosol index. The correspondence of the maxima of the source function and the TOMS index, in the arid and semi-arid regions, is striking.

2.2 Dust Emission

Dust uplifting into the atmosphere is mainly initiated by saltation bombardment (sand blasting). In GOCART, the vertical flux of dust particles is assumed to be proportional to the horizontal flux of sand particles, and it is approximated by an expression similar to the empirical formula developed by *Gillette and Passi* (1988):

$$
F_p = \begin{cases} CSs_p u_{10m}^2 (u_{10m} - u_{tp}) & \text{if } u_{10m} > u_t \\ 0 & \text{otherwise} \end{cases},
\tag{1}
$$

where C is a dimensional factor equal to 1 μg s^2 m^{-5}, S is the source function described by *Ginoux et al.* (2001), u_{10m} is the horizontal wind speed at 10 m, u_{tp} is the threshold velocity for class p, and s_p is the fraction of each size classes given in Table 1.

The threshold velocity for wind erosion is calculated from *Iversen and White* (1982) numerical formulation with the simplications proposed by *Marticorena and Bergametti* (1995). The expression of the threshold velocity for class p, in units of m s^{-1}, is given by

$$
u_{tp} = 0.13 \frac{\sqrt{\frac{\rho_p g \Phi_p}{\rho_a}} \sqrt{1 + \frac{6 \times 10^{-7}}{\rho_p g \Phi_p^{2.5}}}}{\sqrt{1.7638(4.6 \times 10^6 [\Phi_p^{1.56} + 1]^{0.092} - 1)}},
\tag{2}
$$

where ρ_p is the particle density (kg m^{-3}), g is the gravity (9.81 m s^{-2}), Φ_p is the effective diameter of the class p (m), ρ_a is the air density. The values of ρ_p and Φ_p are given for each 4 classes p in Table 1. To take into account the bonding effect of soil moisture, the expression 2 is modified as in *Ginoux et al.* (2001),

$$
u_{twp} = \begin{cases} u_{tp} \times (1.2 + 0.2 \log_{10} w) & \text{if } w < 0.5 \\ \infty & \text{otherwise} \end{cases},
\tag{3}
$$

where w is the soil moisture which varies from near zero values in arid region to 1 for water.

4

3 Model Results

The dust distribution is siumlated from January 1981 to December 1996. The instantaneous dust concentration for each 4 bins at every model grid point is archived every 6 hours.

3.1 Global Budget

Figure 2 shows the global annual budget for 16 years. It includes dust emission and removal by wet and dry deposition. Although the lifetime of dust particles is about 1 week, the annual budget is not equilibrated: the annual deposition by dry and wet deposition is systematically higher than the emission. This is an inherent problem of transport models which cannot conserved mass because of time interpolation. The error is of the order of 1%. Dry deposition contributes for 90% of total dust removal. The ratio between dry and wet removal varies by less than 10% over the 16 years simulation. The maximum difference of annual emission is about 23% with the lowest emission in 1996 (1950 Tg) and the highest in 1988 (2400 Tg).

Table 2 gives the budget over 5 different regions: North Africa, South Africa, North America, South America and Asia. The annual emission from North Africa is around 1400 Tg yr^{-1} which represents 65% of the global emission, while Asia contributes for 25%. The contribution from the other regions is relatively low and of the order of the standard deviation of dust emission from North Africa. Over the 16 years simulation, there is a downward trend of dust emission from Africa and Asia of 6 Tg yr^{-1}, and 2 Tg yr^{-1}. The deposition rates follow the same trends. The difference between the annual rates of emission and deposition gives a measure of dust export from the region. The only region with a negative difference, import from other regions, is North America with about 30 Tg yr^{-1} which is 3 times the amount emitted from this continent. The ratio between dust export and emission gives a measure of the efficiency of source regions to provide dust nutrients the ocean biosphere. The highest efficiency ratio is for Australia (0.3) followed by North Africa (0.2), and the lowest is for Asia (0.1), excluding North America. The major factors affecting the efficiency ratio is the proximity of the sources to the ocean and the altitude and speed of the dust plumes. In Australia, the major dust source is in the Lake Eyre region which is about 600 to 800 km from the Indian Ocean. On the other hand, the most active dust source in Asia (in the Taklamakan desert) is located at more than 3000 km from the Pacific Ocean. Table 3 gives the annual dry and wet deposition rates for 6 oceanic regions. The highest deposition rates are in the North Indian Ocean while the values in the South Indian Ocean is a factor ten lower. The highest contribution of wet deposition is over the North Pacific (50%) and the lowest is over the South Atlantic (10%). Such large difference can be explained by the travel time from the dust source to the ocean. The dust par-

5

ticles deposited in the South Atlantic are coming from Patagonia (Chile) which is bordered by the Atlantic Ocean and from the Makgadikgadi pan (Botswana) which is about 1000 km from the sea shore.

Table 4 gives the winter, summer and annual budgets over Sahara (North of 21.25°N) and Sahel (South of 21.25°N) in North Africa. The emissions from Sahara are twice the corresponding emissions from Sahel, but ther standard deviations are equivalent. This means that there is a stronger inter-annual variability of dust emission over the Sahel. In Sahara, the emissions are 30% higher in summer than in winter, while in Sahel the emissions are slightly higher in winter. In Sahara the wet deposition is negligible compare to the dry deposition, but in Sahel it varies strongly with season: in winter it is negligible but in summer it represents 22% of the removal rate. This can be explained by the movement of the Inter-Tropical Convergence Zone (ITCZ) which occupies its northernmost position in summer. South of the ITCZ, the monsoon carries precipitating clouds. From Table 4, it appears that the inter-annual variability of annual and seasonal emission or deposition rates is different between Sahel and Sahara. The maximum rates in Sahara date for all seasons to 1984, while in Sahel the corresponding year of maximum varies between seasons: 1983 for winter, and 1988 for summer and annual mean. For both regions, the year 1996 has the lowest annual emission. For both regions, there are equivalent downward trends of dust emission.

4 Comparison with In-situ and Remote Sensing Data

4.1 Monthly Climatology of Surface Concentration

Figure 3 shows the comparison between the observed and simulated monthly surface concentration at 16 sites. The results are very similar to the results presented by Ginoux et al. (2001), although they have used a parameterization of u_t which was not appropriate for fine dust but for sand particles. As before, the model is performing correctly in the dusty regions but overestimate dust concentrations in the remote regions of the North hemisphere: over the Atlantic at Mace Head and over the Pacific at Midway. In the South hemisphere, the model results are within the standard deviation of the measurements.

4.2 Inter-annual Variability of Concentration

The surface concentration has been measured for more than 20 years at Barbados and Miami by the University of Miami (Prospero, 1999), and for a decade at Izana by the New Mexico State University (Arimoto et al., 1995). Figure 4 shows

the comparison of the measured and calculated surface concentrations at Izana, Barbados and Miami. The correlations between simulated and observed concentrations are 0.69 for Izana, and 0.79 for Barbados and Miami. The correlations for the monthly anomalies are lower but still significant (99.9% probability of correlation), they are 0.47, 0.56, and 0.31 for Izana, Barbados and Miami.

4.3 TOMS Aerosol Index

The TOMS instrument on board the satellite Nimbus 7 measured aerosol backscattering radiances at 340 and 380 nm from November 1978 until May 1993. In this study, we use the data from the period 1981-1990. These measurements cover the Earth daily with a 50 km resolution at satellite footprint. The local passing time is about 11:30 am. By taking the difference between the measured and calculated radiances for a purely molecular atmosphere, *Herman et al.* (1997) defined the TOMS Aerosol Index (TOMS AI) as follow

$$\text{AI} = -100 \left\{ \log_{10} \left(\frac{I_{340}^m}{I_{380}^m} \right) - \log_{10} \left(\frac{I_{340}^c}{I_{380}^c} \right) \right\}, \tag{4}$$

where I^m is the backscattered radiance measured by TOMS at the given wavelength and I^c is the radiance calculated using a radiative transfer model for a pure Rayleigh atmosphere. The TOMS AI is a qualitative indicator of the presence of UV absorbing aerosols. An inversion procedure that retrieves aerosol properties from the TOMS radiances has been developed by *Torres et al.* (1998). They have shown that for absorbing aerosols, like dust particles, the optical thickness can be derived from the TOMS AI knowing the values of single scattering albedo, the altitude of the aerosol layer, and the surface pressure. Here, an aerosol index is calculated from the satellite viewing angles and the simulated size distribution. The methodology consists to first calculate the optical thickness at 380 nm from the relation:

$$\tau_{380} = \sum_{k=1}^{7} \tau_k = \sum_k \frac{3}{4} \frac{Q_k \alpha_k M_i}{r_k \rho_{pi}} \qquad i{=}1 \text{ for } k \le 4 \text{ and } k = i \text{ for } i > 4 \tag{5}$$

where τ_k is the optical thickness at 380 nm for 7 bins k, Q_k is the extinction efficiency at 380 nm, M_i is the column mass loading of bin i of the 4 transported size bins, α_k is the fraction of each 7 sub-bins, r_k is the effective radius, and ρ_{pi} is the mass density of the size class i. The values of $Q_k(380nm)$ are calculated using Mie theory and using the real and imaginary parts of the refractive index derived by *Colarco et al.* (2002). Second, the single scattering albedo at 380 nm (ω_{380}) is calculated by the relation

$$\omega_{380} = \frac{\sum_{k=1}^{7} \omega_k \tau_k}{\tau_{380}} \tag{6}$$

where ω_k is the single scattering albedo of particle radius r_k and is calculated using Mie theory and the same values of the refractive index as Q_k. The values of r_k, α_k, Q_k, and ω_k are given in Table 5, and the values of ρ_{pi} are given in Table 1. Third, the centroid of mass Z is calculated by the formula

$$Z = \frac{\sum_{j=1}^{nlev} z_j (\sum_{i=1}^{4} C_{i,j}) \Delta z_j}{\sum_i M_i} \tag{7}$$

where z_j is the altitude above ground at level j among the $nlev$ model levels, $C_{i,j}$ is the mass concentration of size class i at level j, Δz_j is the thickness of the grid cell at level j, and M_i is the mass column. With τ_{380}, ω_{380}, Z, and the TOMS instrument viewing angles, an aerosol index is calculated using a look-up table. This table has been built using radiative calculations (*Torres et al.*, 1998) for a limited set of values of $\tau 380$, ω_{380}, Z, and viewing angles. The intermediate values are linearly interpolated.

Figure 5 shows the comparison between the observed and calculated aerosol index during a dust storm from Sahara in March 1988. Around the 27 March 1988, a dust plume was produced from Sahara and transported by the Azores high towards Europe. Two days later, the plume is separating in two branches when West and the other East. The West branch formed two days later an half circle over most of the North Atlantic. The model reproduces the complex pattern of the plume as well as the amplitude of the aerosol index.

The aerosol index has been calculated for the 10 years simulations from January 1981 to December 1989. Figure 6 shows the global distribution of the correlation coefficient between the observed and simulated aerosol index. Over the arid regions the correlation coefficient is higher than 0.8, as well as over the North Atlantic. Over the North Pacific there is a 15 degrees band with significant correlation but most Asian dust plumes are moving eastward at higher latitudes. It is important to understand that the TOMS aerosol index includes all absorbing aerosols including dust and black carbon, while the simulated aerosol index considers only dust particles. So, if the seasonal and inter-annual cycle of the simulated dust distribution is in phase with other absorbing aerosols there will be a positive correlation. Such phase correlations are apparent in the burning regions in South America. When comparing surface dust concentrations at Midway, we showed that the simulated values are overestimated. On the other hand, vertical profiles indicate that the peak of dust concentration is in the upper troposphere, and not at the surface. The TOMS aerosol index increases almost linearly with the plume altitude (*Hsu et al.*, 1999). So, even with relatively small amount, the absorption of solar radiation by aerosols in the upper troposphere can produced higher index than larger amount near the surface. Additional information would be needed to confirm the presence of dust in the upper troposphere over the subtropical Pacific.

5 Effects of North Atlantic Oscillation on Dust Distribution

In this section we examine the inter-annual variability of dust distribution in relation with the North Atlantic Oscillation (NAO). The NAO exerts a strong influence on the large-scale variations of both the atmospheric circulation and the hydrological cycle in the Northern hemisphere. *Hurrell* (1995) have defined a NAO Index which is calculated by taking the difference between normalized sea-level atmospheric pressures between Lisbon, Portugal, and Stykkisholmur, Iceland. Winters with high NAO indices are characterized by a deepening of the Icelandic low associated with a stronger Azores anticyclone. This yields to higher surface pressure and drier conditions over Northern Africa. During low NAO conditions, there is an increase of precipitation over the Mediterranean and North Africa. *Moulin et al.* (1997) have shown that both pattern and intensity of the transport of African dust are affected by the NAO. More recently, *Chiapello et al.* (2002) have confirmed the influence of the NAO on the year-to-year variability of dust export from Africa, using TOMS and Meteosat satellite data.

Figure 7 shows the year-to-year variability of the NAO winter Index values from http://www.cgd.ucar.edu/~jhurrell/nao.html, and the simulated dust concentration at Barbados in Winter and Summer. The correlation between the NAO Index and the winter and summer surface concentration at Barbados are 0.67 and 0.2, respectively. For the other seasons, the correlation is as low as in summer. If one uses the corresponding season for the NAO Index, the correlation does not improve. Mainly because the pressure difference between Iceland and Portugal is much weaker, and thus its effects on the meteorology.

Figure 8 shows the distribution of the correlation coefficient between the NAO winter Index and the winter dust emission, surface concentration and mass column, from 1981 to 1996. There is a high correlation (>0.9) with the dust emission from the Bodele depression-Lake Chad region which is the most active African source in winter (cf. Table 4). The year-to-year variability of surface concentration in winter seems to be correlated with the NAO over much of the North Atlantic and the western part of North Africa. Similar correlation exist for the dust mass column, although with a lesser extend.

The NAO modulates the year-to-year variability of dust emission, but it is unclear if the year-to-year variability of dust distribution is due to the variability of dust emission or transport and\or removal processes.

6 Conclusions

The dust size distribution in the atmosphere is simulated with the GOCART model from 1981 to 1996. The major features of the dust component of the GOCART model are that it is driven by assimilated meteorological fields and the major dust sources are associated with topographic lows. With these characteristics, the model is able to reproduce correctly in-situ and remote sensing measurements, on daily, seasonal and inter-annual scales. The budgets over the different continents and oceans have been compared. Globally, the maximum difference of annual emission from 1981 to 1996 is about 23% with the lowest emission in 1996 (1950 Tg) and the highest in 1988 (2400 Tg). The dust removal by wet deposition contributes globally by only 10% but with important regional variations. Over the North Pacific the wet deposition is about 50% of the total loss. The dust deposition over the Indian Ocean (northern hemisphere) is as important, annualy, than over the North Atlantic. The annual mean North African emission is about 1400 Tg which corresponds to 65% of the global emission. The second major dust source region is East Asia which contributes for 25%. Although North America has active dust sources in the South-west, it constitutes a sink for dust by about 30 Tg yr^{-1}. In North Africa and East Asia, there is a downward trend of dust emission of 6 and 2 Tg yr^{-1}, respectively. Dust emission shift from Sahel and Sahara following the seasonality of the ITCZ. In winter, when the ITCZ occupies its southernmost position, most emission is from Sahel. In summer the northward displacement of the ITCZ is accompanied with precipitation over the Sahel and the dry Sahara is by then the principal dust source. Both regions present different inter-annual variability but they both show a downward trend of dust emission. The inter-annual variability of dust distribution and emission is compared with the NAO Index. It is showed that the winter surface concentration is strongly correlated with the NAO Index over much of the North Atlantic and western Africa. We find a high correlation between the NAO Index and dust emission from the Bodele depression- Lake Chad region. But is unclear if the year-to-year variability of surface concentration is related to dust emission or to transport and\or removal processes. In order to differentiate the contribution from the different processes, it would be necessary to realize simulations with constant transport and removal processes. Also, longer simulations should be realized to support the strong relation between dust distribution in winter and the NAO.

References

Arimoto, R., R. A. Duce, B. J. Ray, W. G. Ellis Jr., J. D. Cullen, and J. T. Merrill, 1995, Trace elements in the atmosphere over the North Atlantic, J. Geophys. Res., 100, 1199-1213.

Chiapello, I. and C. Moulin, 2002, TOMS and METEOSAT satellite records of the

variability of Saharan dust transport over the Atlantic during the last two decades (1979-1997), Geophys. Res. Lett., 29, 10.1029/ 2001GL013767.

Chin, M., R. B. Rood, S.-J. Lin, J.-F. Müller, and A. Thompson, 2000, Atmospheric sulfur cycle simulated in the global model GOCART: Model description and global properties, J. Geophys. Res., 105, 24,671-24,687.

Chin, M., P. Ginoux, S. Kinne, O. Torres, B. Holben, B. N. Duncan, R. V. Martin, J. Logan, A. Higurashi, and T. Nakajima, 2002, Tropospheric aerosol optical thickness from the GOCART model and comparisons with satellite and sun photometer measurements, J. Atmos. Phys., 59, 461-483.

Colarco, P. R., O. B. Toon, O. Torres, and P. J. Rasch, 2002, Determining the UV imaginary index of refraction of Saharan dust particles from TOMS data and a three dimensional model of dust transport, J. Geophys. Res., in press.

Dentener, F. J., G. R. Carmichael, Y. Zhang, J. Lelieveld, and P. J. Crutzen, 1996, Role of mineral aerosol as a reactive surface in the global troposphere, J. Geophys. Res, 101, 22,869-22889.

Dickerson, R. R., S. Kondragunat, G. Stenchikov, K. L. Civerolo, B. G. Doddridge, and B. N. Holben, 1997, The impact of aerosols on solar ultraviolet radiation and photochemical smog, Science, 278, 827-830.

Dubovik, O., B. Holben, T. F. Eck, A. Smirnov, Y. J. Kaufman, M. D. King, D. Tanré, and I. Slutsker, Variability of absorption and optical properties of key aerosol types observed in worldwide locations, *J. Atmos. Sci., 59*, 590-608, 2002.

Gillette, D. A., and R. Passi, 1988, Modeling dust emission caused by wind erosion, *J. Geophys. Res., 93*, 14,233-14,242.

Ginoux, P., M. Chin, I. Tegen, J. M. Prospero, B. Holben, O. Dubovik, and S. J. Lin, 2001, Sources and distributions of dust aerosols simulated with the GOCART model, J. Geophys. Res., 106, 20,255-20,274.

Griffin, D. W., V. H. Garrison, J. R. Herman, and E. A. Shinn, 2001, African desert dust in the Caribbean atmosphere: microbiology and public health, Aerobiologia, 17(3), 203-213.

Herman, J. R., P. K. Bhartia, O. Torres, C. Hsu, C. Seftor, and E. Celarier, 1997, Global distribution of UV-absorbing aerosols from Nimbus 7/TOMS data, J. Geophys. Res., 102, 16,911-16,922.

Hurrell, J. W., 1995, Decadal trend in the North Atlantic Oscillation: Regional temperatures and precipitations, Science, 269, 676-679.

Hsu, N. C., J. R. Herman, O. Torres, B. N. Holben, D. Tanré, T. F. Eck, A. Smirnov, B. Chatenet, and F. Lavenu, 1999, Comparisons of the TOMS aerosol index with sun-photometer aerosol optical thickness: Results and applications, J. Geophys. Res., 104, 6269-6279.

Iversen, J. D., and B. R. White, 1982, Saltation threshold on Earth, Mars and Venus, Sedimentology, 29, 111-119.

Liao, H., Y. L. Yung, and J. H. Seinfeld, 1999, Effects of aerosols on tropospheric photolysis rates in clear and cloudy atmospheres, J. Geophys. Res., 104, 23,697-23,707.

Marticorena B., and G. Bergametti, 1995, Modeling the atmospheric dust cycle: 1. Design of a soil-derived dust emission scheme, J. Geophys. Res., 100, 16,415-

16,430.

Martin, J. H. and R. M. Gordon, 1988, Northeast Pacific iron distributions in relation to phytoplankton productivity, Deep-Sea Res., 35, 177-196.

Martin, R.V., D.J. Jacob, J.A. Logan, I. Bey, R.M. Yantosca, A.C. Staudt, Q. Li, A.M. Fiore, B.N. Duncan, H. Liu, P. Ginoux, and V. Thouret, 2002, Interpretation of TOMS observations of tropical tropospheric ozone with a global model and in-situ observations, J. Geophys. Res., in press.

Moulin, C., C. E. Lambert, F. Dulac, and U. Dayan, 1997, Control of atmospheric export of dust from North Africa by the North Atlantic Oscillation, Nature, 387, 691-694.

Prospero, J. M., R. Schmitt, E. Cuevas, D. L. Savoie, W. C. Graustein, K. K. Turekian, A. Volz-Thomas, A. Diaz, S. J. Oltmans, and H. Levy II, 1995, Temporal variability of summer-time ozone and aerosols in the free troposphere over the eastern North Atlantic, Geophys. Res. Lett., 22, 2925-2928.

Prospero, J. M., 1999, Long-term measurements of the transport of African mineral dust to the Southeastern United States: Implications for regional air quality, J. Geophys. Res., 104, 15,917-15,927.

Prospero, J. M., P. Ginoux, O. Torres, S. Nicholson, and T. Gill, 2002, Environmental characterization of global sources of atmospheric soil dust derived from the nimbus 7 total ozone mapping spectrometer (TOMS) absorbing aerosol product, Rev. of Geophys., 40(1), 1002, doi:10.1029/2000RG000095.

Schubert, S. D., R. B. Rood, and J. Pfaendtner, 1993, An assimilated data set for earth science applications, Bull. Am. Meteorol. Soc., 74, 2331-2342.

Sokolik, I. N. and O. B. Toon, 1996, Direct radiative forcing by anthropogenic airborne mineral aerosol, Nature, 381, 681-683.

Tegen, I., and A. A. Lacis, 1996, Modeling of particle size distribution and its influence on the radiative properties of mineral dust aerosol, J. Geophys. Res., 101, 19,327-19,244.

Torres, O., P. K. Bhartia, J. R. Herman, Z. Ahmad, and J. Gleason, 1998, Derivation of aerosol properties from satellite measurements of backscattered ultraviolet radiation: Theoretical basis, J. Geophys. Res., 103, 17099-17,110.

Torres, O., P. K. Bhartia, J. R. Herman, A. Sinyuk, P. Ginoux, and B. Holben, 2002, A long-term record of aerosol optical depth from TOMS observations and comparison to AERONET measurements, J. Atmos. Sciences, 59, 398-413.

Weaver, C., P. Ginoux, N. Hsu, M-D. Chou, and J. Joiner, 2002, Radiative forcing of Saharan dust: GOCART model simulations compared with ERBE data, J. Atmos. Sciences, 59, 736-747.

Source function
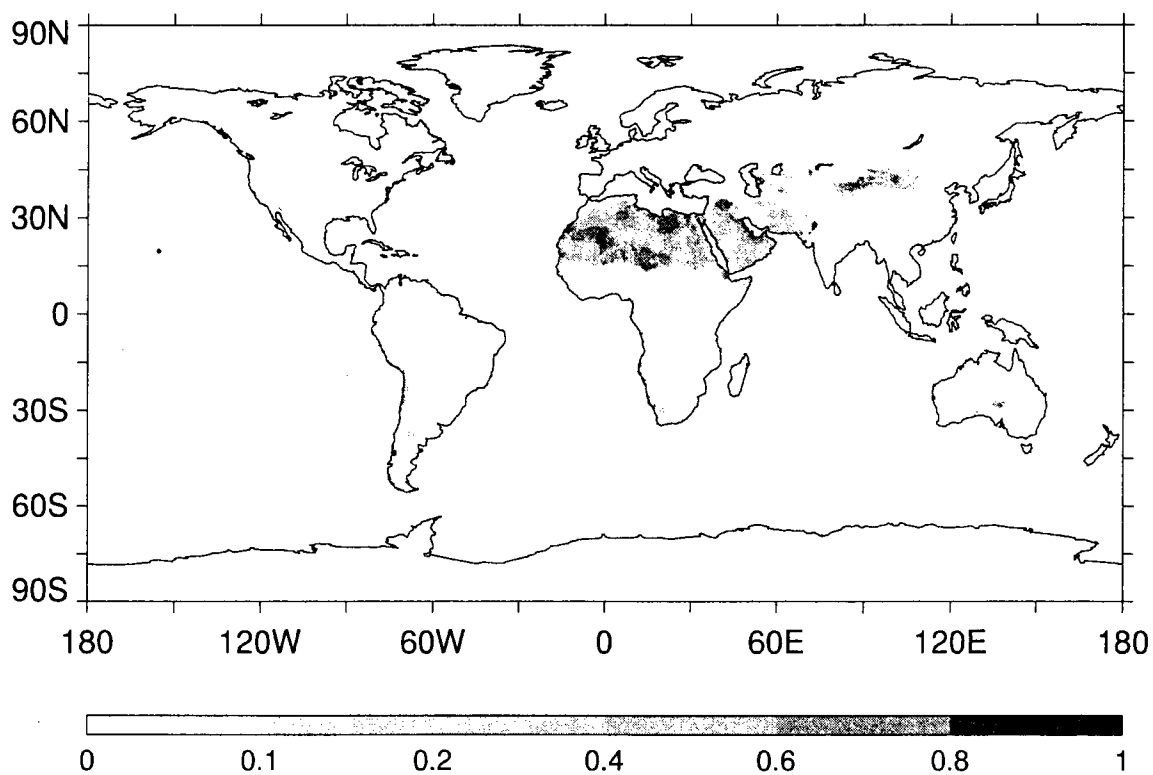
TOMS Aerosol Index
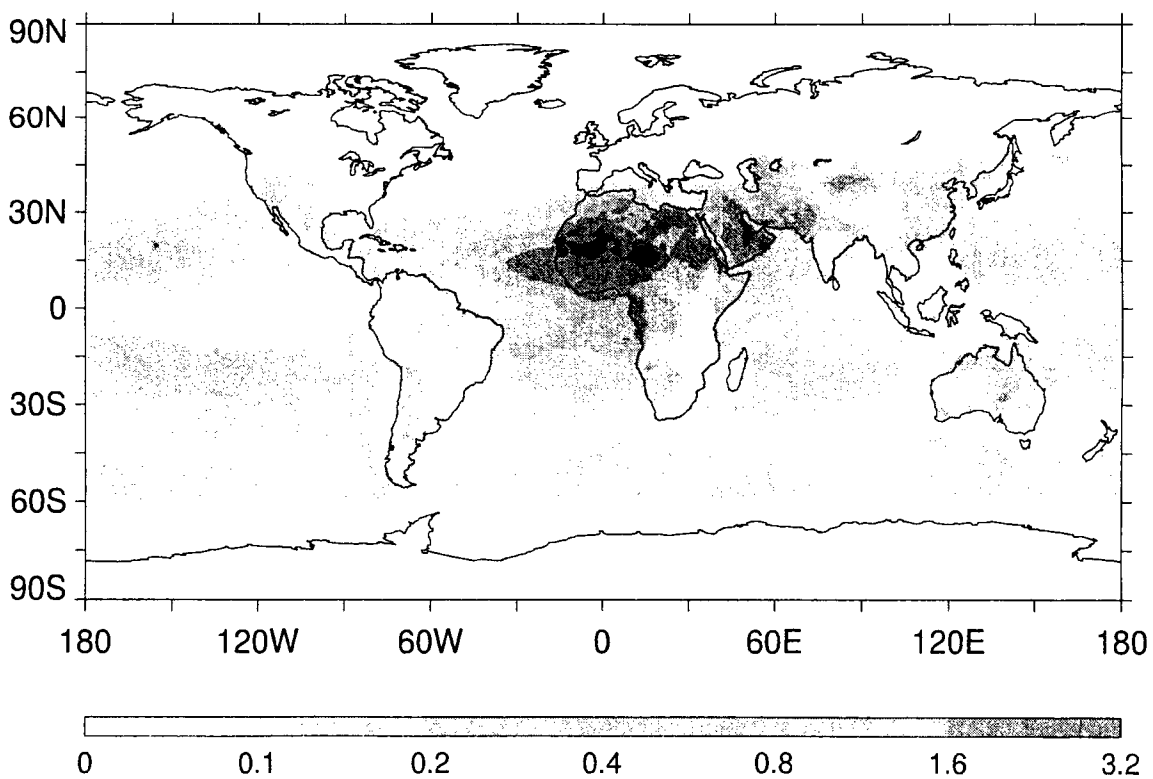
Fig. 1. Global distribution of the dust sources on GOCART grid

Table 1

Physical Properties of the Transported Size Bins

Bin	Radius Range	Size Distribution	Source fraction	r_i,	ρ_{pi}
	μm			μm	kg m^{-3}
1	0.1 - 1	$\frac{dm}{d\ln r}$=cst	0.1	0.75	2600
2	1 - 2	$\frac{dm}{dr}$=cst	0.25	1.5	2600
3	2 - 3	$\frac{dm}{dr}$=cst	0.25	2.5	2600
4	3 - 6	$\frac{dm}{dr}$=cst	0.25	4.5	2600
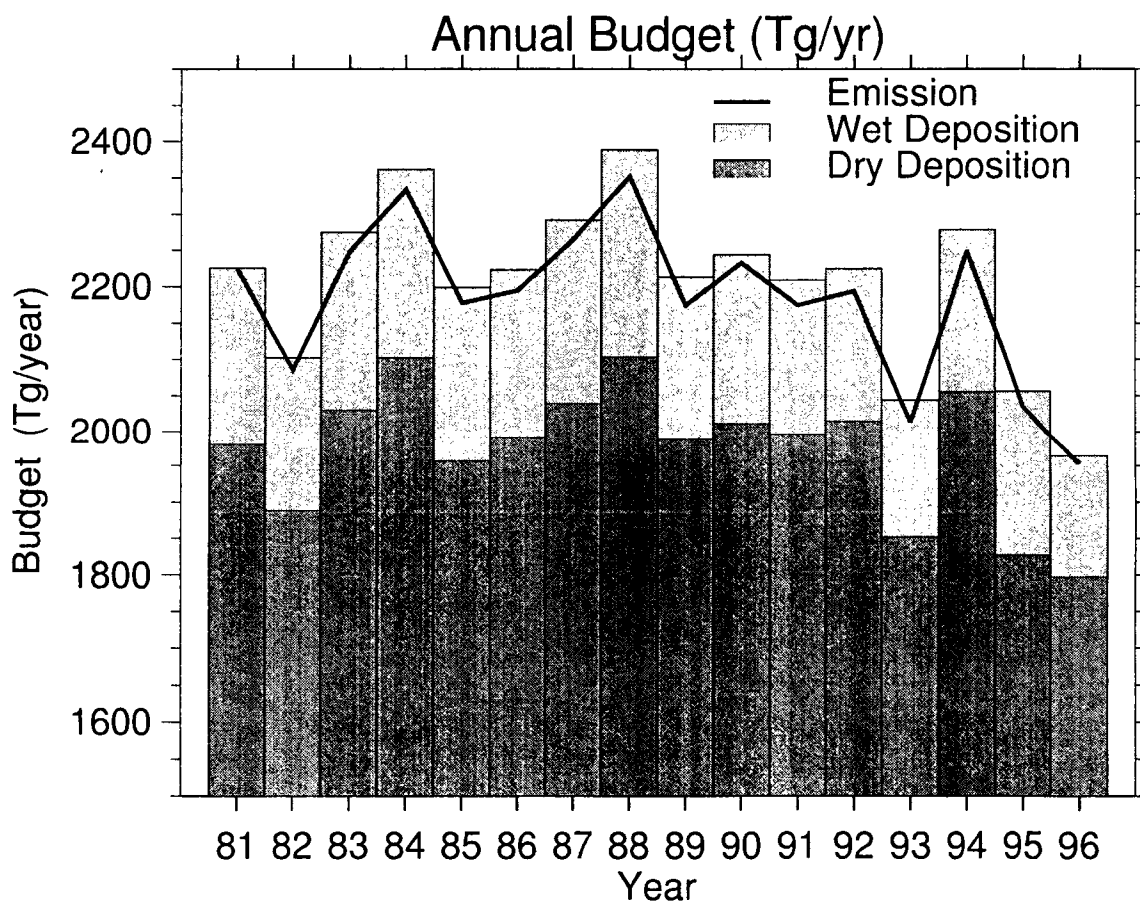
Fig. 2. Global Annual Budget of Dust from 1981 to 1996: Emission (line), dry deposition (dark gray boxes), and wet deposition (light gray boxes), in units of Tg yr^{-1}.

14
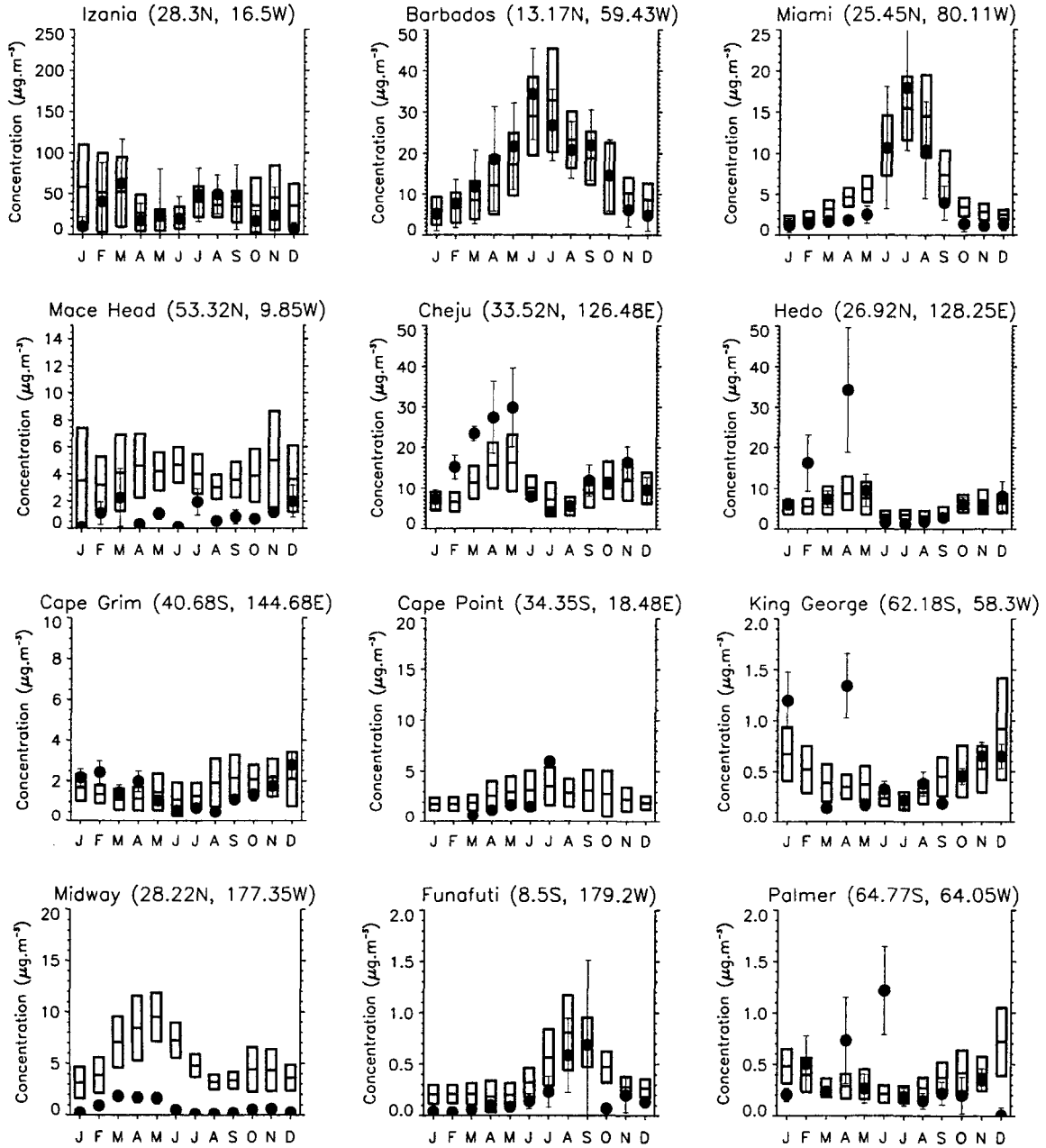
Fig. 3. Comparison of the climatological monthly surface concentration, simulated (boxes) and observed (dots) at 12 sites in units of μg m^{-3}, with their standard deviation.
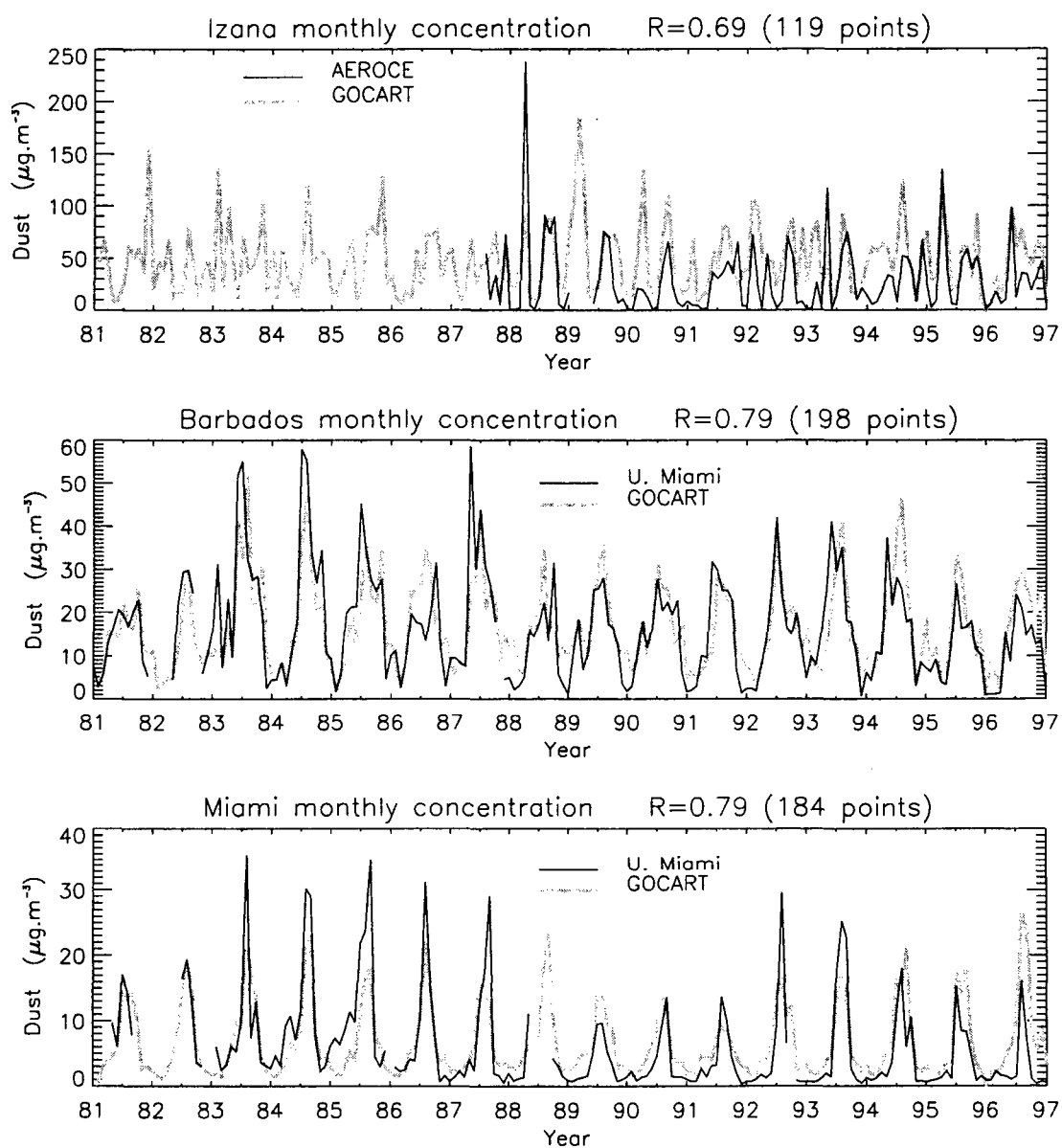
Fig. 4. Monthly dust concentration from January 1981 to December 1996, simulated (gray line) and observed (iblack line) at Izana (upper panel), Barbados (middle panel), and Miami (lower panel), in units of μg m^{-3}.

TOMS Absorbing Aerosol Index

GOCART Aerosol Index
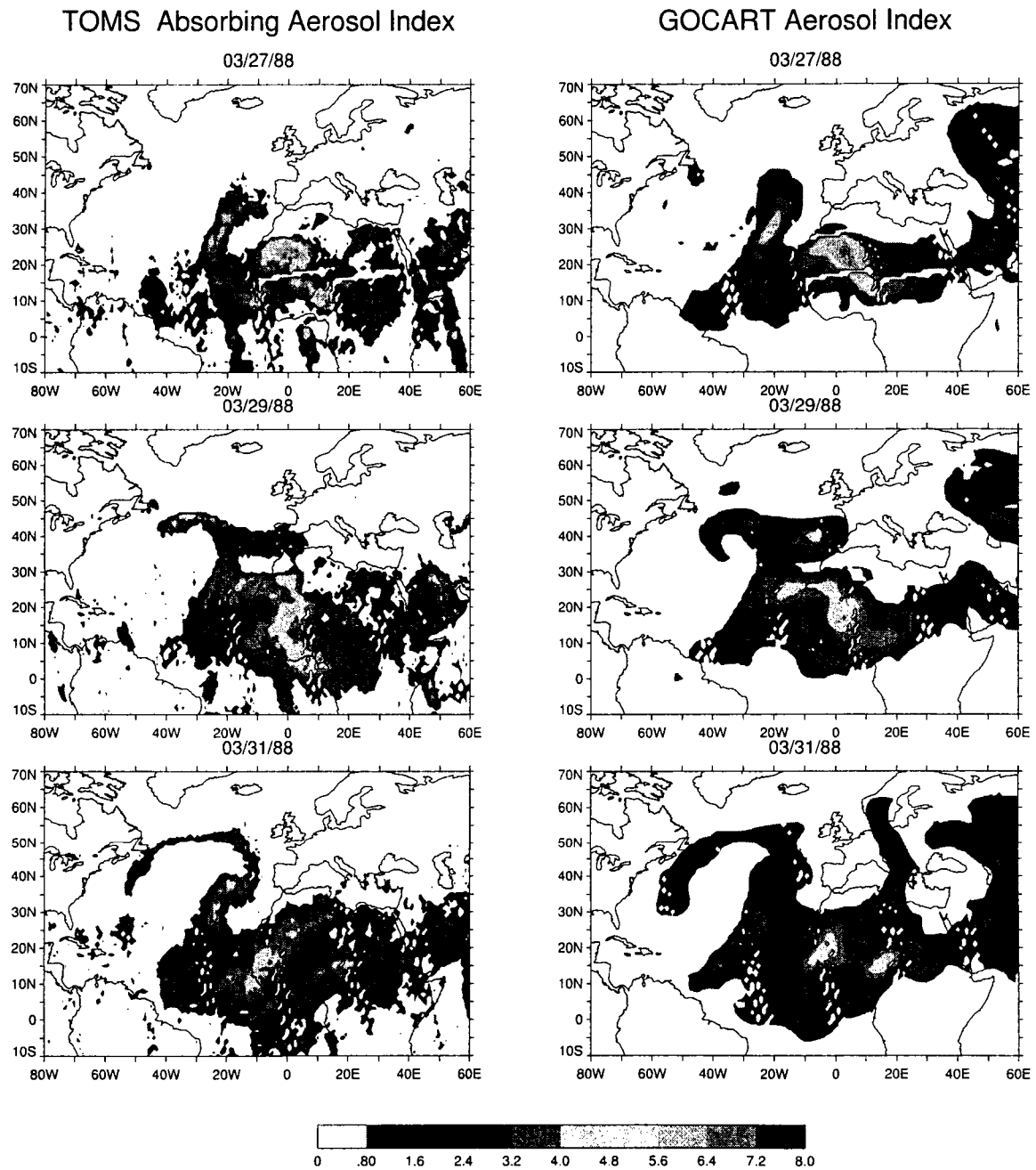
Fig. 5. Comparison between the TOMS absorbing aerosol index (left panels) and simulated index (right panels) during the evolution of a dust plume over the North Atlantic in March 1988.

17
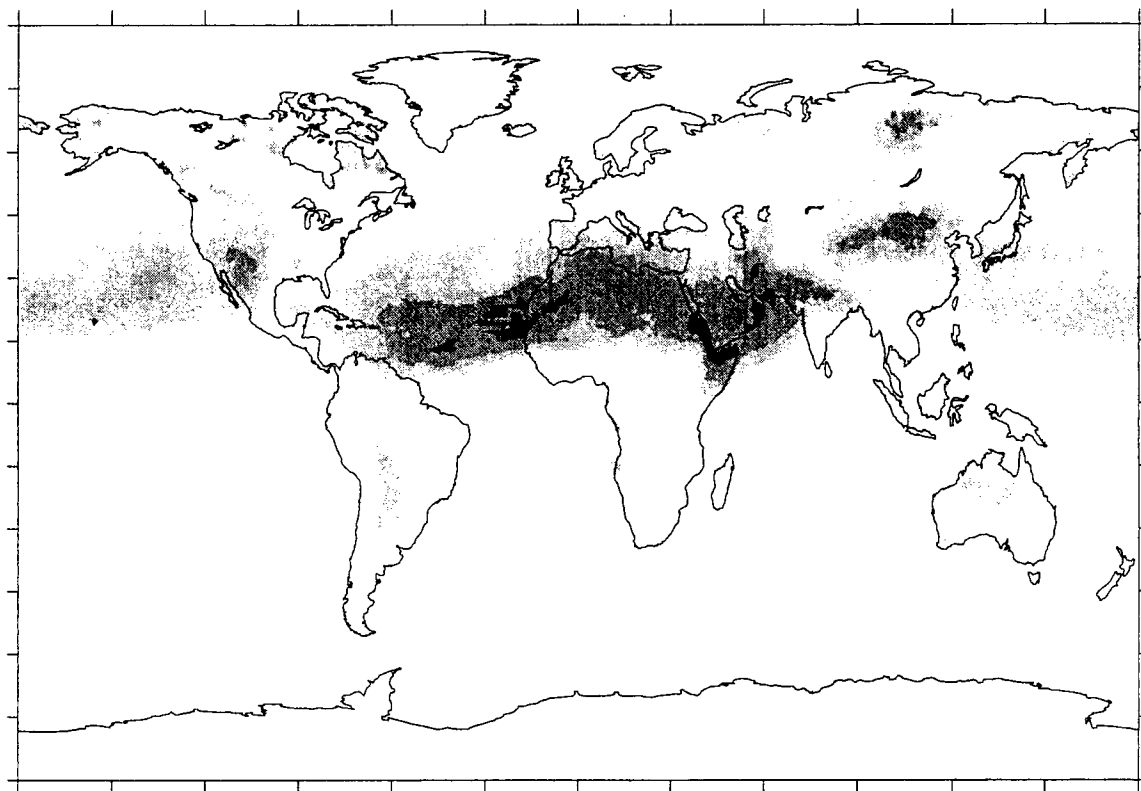
Correlation Coefficient R=(TOMS AI,GOCART Index)

| 0 | 0.500 | 0.600 | 0.700 | 0.800 | 0.900 | 1.00 |
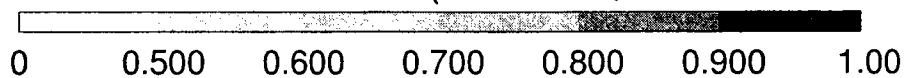
Fig. 6. Global distribution of the correlation coefficient between the TOMS aerosol index and an index calculated with the model results and TOMS viewing angles from January 1981 to December 1990.
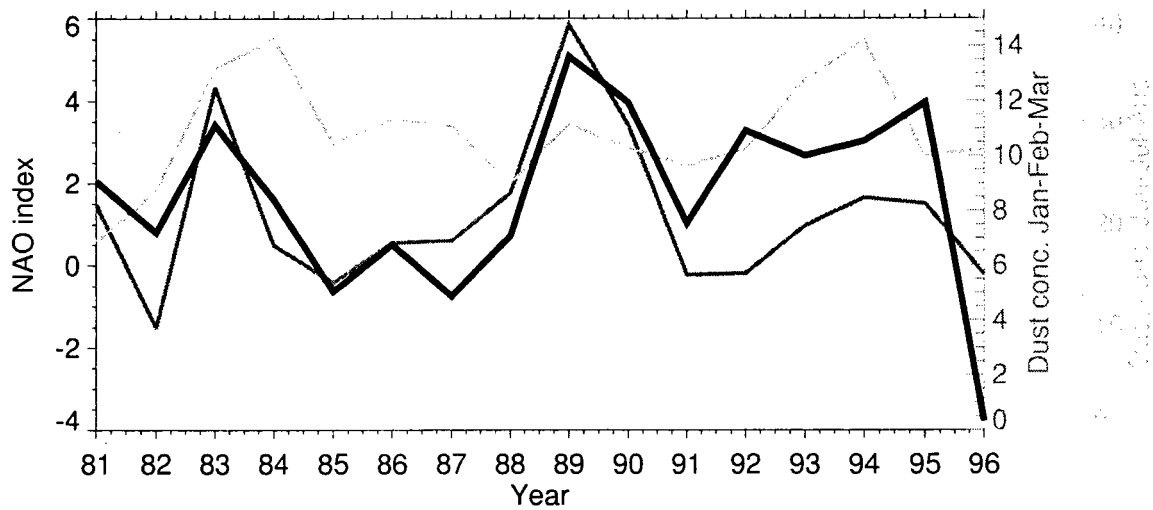
Fig. 7. Comparison between NAO Index (bold black) and surface concentration at Barbados in Winter (dark gray) and Summer (light gray) from 1981 to 1996 in units of μg m^{-3}.
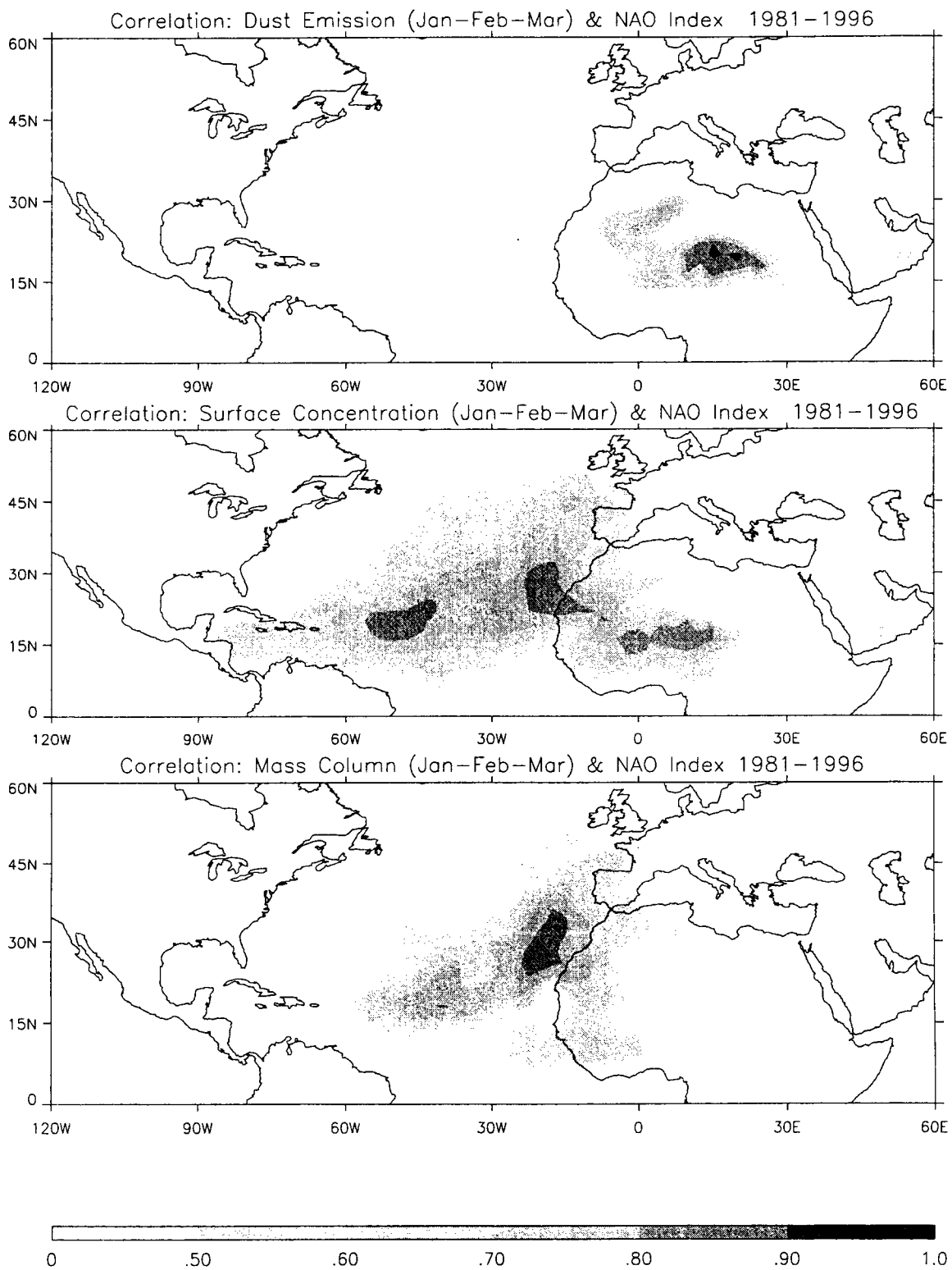
Fig. 8. Global distribution of the correlation coefficient between the NAO Index and the winter (Jan-Feb-Mar) mean dust emission (upper panel), surface concentration (middle panel), and mass colum (lowere panel), from 1981 to 1996.

Table 2. Annual Budget over Six Continents in units of Tg yr−1

Year	N Africa Emi	Dry	Wet	Exp	S Africa Emi	Dry	Wet	Exp	N America Emi	Dry	Wet	Exp	S America Emi	Dry	Wet	Exp	Asia Emi	Dry	Wet	Exp	Australia Emi	Dry	Wet
1981	1461	1067	81	312	26	20	1	4	9	28	11	-30	49	37	4	9	506	419	28	59	61	44	2
1982	1369	1028	62	279	23	18	1	4	10	29	10	-30	48	35	4	9	472	397	25	50	59	43	1
1983	1507	1107	64	336	22	17	1	4	8	31	13	-36	56	41	6	9	484	397	30	58	55	40	2
1984	1538	1120	66	352	24	19	1	3	10	34	15	-39	53	40	7	7	525	434	29	61	58	42	2
1985	1408	1037	67	304	22	17	1	4	10	30	12	-33	51	38	5	8	504	416	27	60	67	46	3
1986	1397	1044	59	294	23	17	1	4	9	30	13	-34	55	38	5	12	533	430	31	73	60	44	2
1987	1459	1079	69	312	27	21	2	4	9	32	13	-36	56	41	6	9	528	432	26	71	67	46	2
1988	1544	1121	76	347	19	17	2	0	11	35	14	-37	61	43	6	12	516	426	36	54	71	49	2
1989	1416	1065	60	291	21	17	1	3	10	32	12	-33	57	40	5	12	488	399	27	63	53	39	2
1990	1446	1085	50	311	20	16	1	3	10	28	11	-29	61	42	5	14	502	404	40	58	65	45	2
1991	1380	1056	51	273	19	16	1	2	9	32	11	-34	56	39	5	12	517	420	33	64	63	45	2
1992	1466	1085	54	328	20	16	1	3	8	31	11	-34	49	36	4	9	488	423	24	42	58	43	2
1993	1350	1019	52	278	22	17	1	4	7	25	10	-27	65	45	5	15	398	343	22	32	57	41	2
1994	1431	1053	49	329	21	18	1	3	9	34	13	-38	58	42	5	11	530	438	33	58	64	44	2
1995	1415	1063	68	284	19	17	1	2	7	28	12	-32	56	41	5	11	504	416	27	60	71	48	2
1996	1288	971	36	281	24	19	1	4	8	32	11	-36	44	33	4	7	435	355	19	62	52	39	1
Mean	1430	1062	60	307	22	17	1	3	9	31	12	-34	55	39	5	10	496	409	29	58	61	44	2
Dev	66	38	11	25	2	1	0	1	1	3	1	3	5	3	1	2	35	26	5	10	6	3	0
Trend	-6	-3	-2	-2	0	0	0	0	0	0	0	0	0	0	0	0	-2	-2	0	0	0	0	0

21

Table 3
Annual Budget over Six Oceans in units of Tg yr−1

Year	N Atlantic		S Atlantic		N Pacific		S Pacific		N Indian		S Indian	
	Dry	Wet	Dry	Wet	Dry	Wet	Dry	Wet	Dry	Wet	Dry	Wet
1981	117	32	17	2	76	39	20	5	126	37	12	3
1982	101	28	15	2	74	37	20	4	118	36	11	3
1983	148	39	17	3	81	39	20	5	120	38	11	4
1984	135	39	18	3	88	45	22	6	145	42	13	4
1985	119	36	16	3	73	41	23	6	129	36	13	4
1986	129	30	19	2	77	42	22	5	128	38	13	3
1987	124	43	20	3	85	42	25	6	123	35	14	4
1988	130	42	21	4	85	44	27	8	140	47	15	5
1989	137	31	19	3	77	38	21	5	133	38	12	3
1990	133	32	20	2	70	37	24	5	132	44	12	3
1991	117	25	20	2	82	38	24	5	134	38	12	3
1992	144	30	14	2	83	39	20	5	117	35	10	3
1993	130	29	17	2	63	32	22	4	119	30	12	3
1994	144	23	18	3	86	45	24	5	140	40	14	4
1995	124	40	16	2	75	38	23	5	119	36	12	3
1996	112	24	18	1	78	38	22	4	111	25	12	2
Mean	128	33	18	2	78	39	23	5	127	37	12	3
Dev	12	6	2	1	6	3	2	1	9	5	1	1
Trend	0	-1	0	0	0	0	0	0	0	0	0	0

Table 4. Winter (January-March), Summer (June-August) and Annual Budget over Sahara (latitude >21.25°N) and Sahel (latitude <21.25°N)

Year	Sahara												Sahel											
	Jan-Feb-Mar (Tg 3mth^{-1})				Jun-Jul-Aug (Tg 3mth^{-1})				Annual (Tg yr^{-1})				Jan-Feb-Mar (Tg 3mth^{-1})				Jun-Jul-Aug (Tg 3mth^{-1})				Annual (Tg yr^{-1})			
	Emi	Dry	Wet	Exp	Emi	Dry	Wet	Exp	Emi	Dry	Wet	Exp	Emi	Dry	Wet	Exp	Emi	Dry	Wet	Exp	Emi	Dry	Wet	E
1981	215	138	1	76	301	176	4	121	940	602	9	328	158	141	2	14	122	107	40	-25	520	465	72	-
1982	187	132	1	53	287	169	4	114	875	591	10	275	150	125	2	23	125	112	32	-18	493	438	52	.
1983	219	143	1	75	298	173	3	121	934	602	7	324	184	161	1	22	134	120	35	-21	574	505	57	1
1984	229	149	1	80	319	180	3	136	987	629	8	349	165	152	3	10	152	127	35	-11	551	491	58	
1985	200	139	0	61	274	158	3	114	878	573	8	297	147	130	2	15	133	113	35	-15	530	464	59	
1986	200	136	0	64	275	161	3	111	885	574	7	304	141	131	3	7	138	117	31	-10	512	470	52	-
1987	202	137	1	64	279	167	4	108	895	595	8	292	140	129	2	9	137	118	36	-16	564	483	61	2
1988	226	153	0	73	313	179	4	130	957	624	9	324	174	150	3	22	163	128	43	-8	587	497	67	2
1989	230	152	0	77	262	158	3	102	875	585	6	285	182	157	2	24	128	118	34	-23	541	480	54	.
1990	204	143	0	60	265	158	1	106	881	594	4	283	179	154	2	23	134	116	27	-10	565	491	46	2
1991	196	141	1	55	265	162	2	101	876	601	6	269	143	129	1	13	140	120	29	-10	504	454	45	.
1992	195	143	0	52	278	166	3	110	908	603	7	299	167	142	1	23	141	122	32	-12	558	482	47	2
1993	177	129	1	47	269	160	2	106	831	568	7	256	163	135	2	26	126	111	27	-13	519	451	45	2
1994	224	149	0	75	280	163	2	116	902	584	6	312	162	145	2	15	134	112	26	-4	528	468	43	1
1995	190	127	1	62	290	169	3	118	869	565	8	296	159	143	1	14	136	117	38	-19	509	456	59	-
1996	177	126	0	51	279	170	1	107	854	570	2	281	117	106	1	9	111	102	22	-12	435	401	34	.
Mean	204	140	1	64	283	167	3	114	897	591	7	298	158	139	2	17	135	116	33	-14	531	468	53	
Dev	17	8	0	10	16	7	1	9	39	18	2	24	17	14	1	6	11	7	5	6	36	25	9	1
Trend	-1	0	0	-1	-2	-1	0	-1	-5	-2	0	-2	-1	-1	0	0	0	0	-1	1	-3	-2	-1	1

23

Table 5

Optical Properties of Dust Particles Used to Calculate an Aerosol Index: Effective Radius (r_k) of the sub-bin k of the 4 transported bins (Bin), size fraction of the sub-bin (Fraction), Exctinction Efficiency at 380 nm (Q_k), and Single Scattering ALbedo at 380 nm (ω_k).

k	r_k	Bin	Fraction	$Q_k(380nm)$	$\omega_k(380nm)$
	μm				
1	0.14	1	0.01	0.732	0.962
2	0.24	1	0.08	0.276	0.976
3	0.45	1	0.25	3.975	0.968
4	0.8	1	0.65	2.427	0.905
5	1.5	2	1	2.354	0.861
6	2.5	3	1	2.228	0.798
7	4.5	4	1	2.182	0.725